

Electronic Supporting Information for

Accessing the triplet state of perylene-3,4,9,10-tetracarboxylic diimide by radical-enhanced intersystem crossing

Maximilian Mayländer,¹ Oliver Nolden,² Michael Franz,¹ Su Chen,³ Laura Bancroft,³
Yunfan Qiu,³ Michael R. Wasielewski,³ Peter Gilch,² Sabine Richert^{1*}

¹ *Institute of Physical Chemistry, University of Freiburg, Albertstraße 21, 79104 Freiburg, Germany*

² *Institute of Physical Chemistry, Heinrich Heine University Düsseldorf, Universitätsstraße 1,
40225 Düsseldorf, Germany*

³ *Department of Chemistry, Center for Molecular Quantum Transduction, and Institute for
Sustainability and Energy at Northwestern, Northwestern University, 2145 Sheridan Road, Evanston,
IL 60208-3113, United States*

* E-mail: sabine.richert@physchem.uni-freiburg.de

Table of Contents

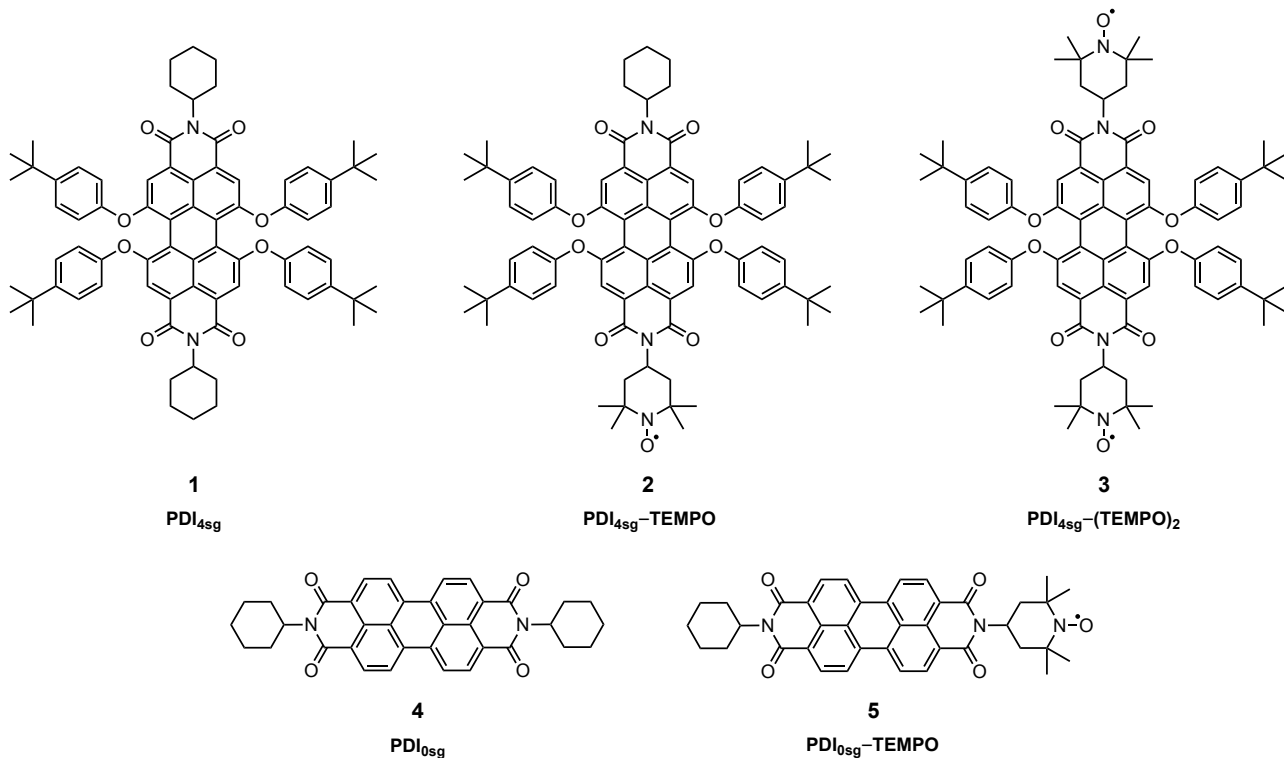
1	Synthesis of the PDI–TEMPO compounds	S1
2	UV-vis characterization	S3
2.1	UV-vis absorption spectra of the PDI–TEMPO compounds	S3
2.2	Time-correlated single photon counting	S3
2.3	Calculation of the radiative rate constant using the Strickler-Berg equation	S4
2.4	Calculation of the Förster energy transfer rate constant	S4
3	Additional fsTA data and global kinetic analysis	S6
3.1	TA data for the PDI _{4sg} -based compounds	S6
3.2	Global kinetic analysis	S6
3.3	Triplet yield determination from the fsTA data	S7
3.4	Influence of the solvent	S9
3.5	Calculation of the driving forces for electron transfer	S12
4	Additional EPR data	S14
4.1	Quantitative EPR on PDI _{4sg} –TEMPO and PDI _{4sg} –(TEMPO) ₂	S14
4.2	Transient nutation data for PDI _{4sg} –(TEMPO) ₂	S14
4.3	Double electron-electron resonance experiments on PDI _{4sg} –(TEMPO) ₂	S14
5	DFT calculations	S16
5.1	TD-DFT calculations	S16
5.2	Calculation of the magnetic properties	S17

List of Figures

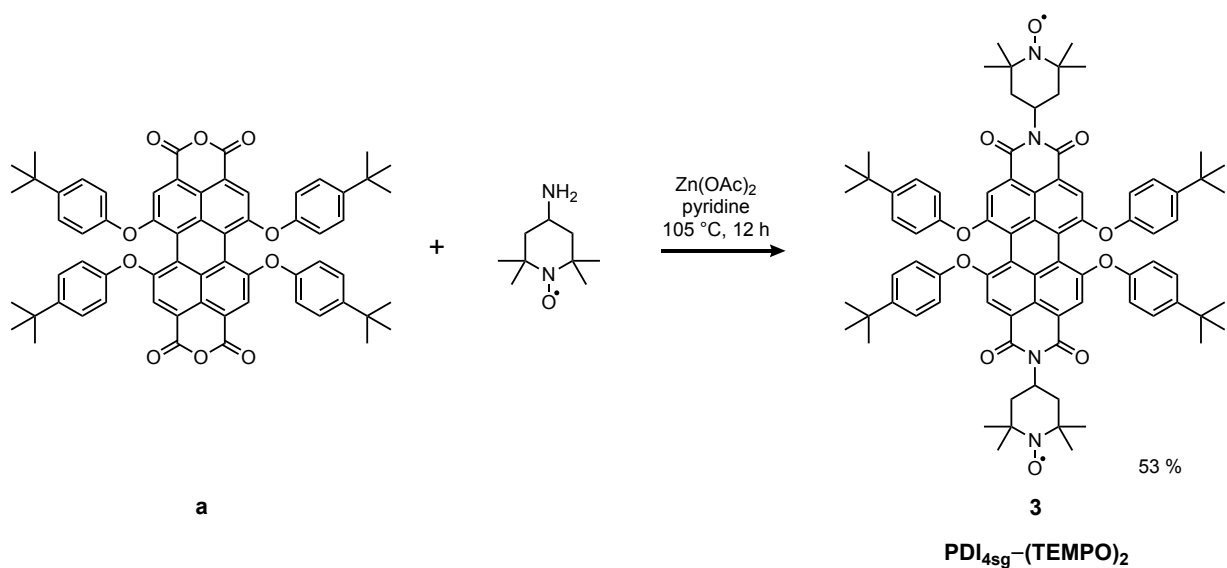
S1	UV-vis absorption spectra of the PDI–TEMPO compounds	S3
S2	Time-correlated single photon counting traces for PDI _{0sg} and PDI _{4sg}	S3
S3	UV-vis absorption spectrum of the TEMPO radical	S4
S4	Contour plots of the fsTA data of the PDI _{4sg} -based compounds	S6
S5	Decay associated spectra for the PDI–TEMPO compounds	S7
S6	Decay associated spectra for PDI _{4sg} –(TEMPO) ₂	S7
S7	Triplet yield determination for PDI _{0sg} –TEMPO	S8
S8	Contour plots of the fsTA data of the PDI–TEMPO compounds in 2-methyltetrahydrofuran	S9
S9	Femtosecond TA spectra and kinetics in 2-methyltetrahydrofuran	S10
S10	DAS for the PDI–TEMPO compounds in 2-methyltetrahydrofuran	S11
S11	DAS for PDI _{4sg} –(TEMPO) ₂ in 2-methyltetrahydrofuran	S11
S12	Femtosecond TA data of PDI _{4sg} –TEMPO using an extended spectral detection window	S11
S13	Quantitative EPR on PDI _{4sg} –(TEMPO) ₂	S14
S14	Transient nutation frequency map for PDI _{4sg} –(TEMPO) ₂	S15
S15	DEER data and analysis for PDI _{4sg} –(TEMPO) ₂	S15
S16	HOMO/LUMO orbitals of the PDIs	S16
S17	Spin densities of the PDI triplet states	S17
S18	Spin densities of the doublet and quartet states of PDI–TEMPO	S18
S19	Spin densities of the triplet and quintet states of PDI _{4sg} –(TEMPO) ₂	S18

1 Synthesis of the PDI-TEMPO compounds

All chemicals were purchased from Sigma-Aldrich, Inc. unless noted otherwise. ^1H NMR spectra were acquired using a 400 MHz Bruker Avance III HD NMR. Mass spectra were collected using a Bruker RapiFlex MALDI-TOF. Purification was performed using silica gel from Sorbent Technologies (Atlanta, GA).



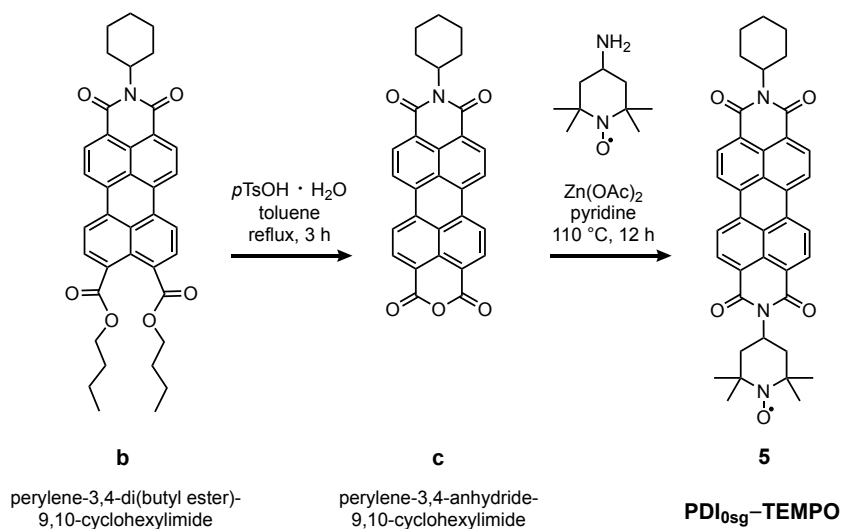
Compounds **1**, **2** and **4** were synthesized according to literature procedures [1, 2, 3, 4].



Compound **a** was synthesized according to the literature [5]. A 25 ml two-necked bottle was charged with a stir bar, and compound **a** (30 mg, 0.03 mmol), 4-amino-TEMPO (26 mg, 0.15 mmol), pyridine (2 ml), and $\text{Zn}(\text{OAc})_2$ (1 mg, 0.005 mmol) were added. The two-necked bottle was then connected to a

condenser with running water. The reaction mixture was heated to 105 °C and stirred for 12 hours. The solvent was then evaporated, and the product was purified by column chromatography (1–2 % acetone in DCM). 20.5 mg of **3** was obtained in 53 % yield.

MALDI-TOF: calculated for $[M]^-$ $m/z = 1290.666$, found 1290.642. R_f 0.7 (5 % acetone in DCM).



Compound **b** was synthesized according to the literature and NMR spectra matched those reported previously [6, 7, 8]. In a flame-dried round bottle flask, **b** (120 mg, 0.2 mmol), *p*-toluene sulfonic acid monohydrate (57 mg, 0.3 mmol), and toluene (3 mL) were added with a magnetic stirring bar. The combined mixture was refluxed under nitrogen for 3 hours until an insoluble dark red solid appeared. The solvent was then removed and the remaining solid **c** (84 mg, 0.18 mmol, 89 % yield) was isolated by vacuum filtration and washed three times with methanol before dried under vacuum. ¹H-NMR was not acquired due to poor solubility of **c**.

MS (MALDI-TOF) m/z : $[M]^-$ calculated $C_{30}H_{19}NO_5$, 473.48; found 473.26.

In a flame-dried 25 mL two-necked round bottle flask, **c** (47 mg, 0.1 mmol), 4-amino-TEMPO (21 mg, 0.12 mmol), and a catalytic amount of $Zn(OAc)_2$ (2 mg, 0.01 mmol) were combined with a magnetic stirring bar. The mixture was purged three times and filled with nitrogen before pyridine (3 mL) was added. The resulting suspension was heated at 110 °C for 12 hours and yielded a nearly homogenous solution. The solvent was evaporated and the crude product was submitted to column chromatography (methanol:DCM 1:99 as eluent). 27 mg of the target molecule **5** were obtained in 36 % yield.

MS (MALDI-TOF) m/z : $[M]^-$ calculated $C_{39}H_{36}N_3O_5$, 626.73; found 626.24.

2 UV-vis characterization

2.1 UV-vis absorption spectra of the PDI-TEMPO compounds

Figure S1 shows the UV-vis absorption spectra recorded for the different PDI-TEMPO compounds in toluene solution at room temperature. The absorption of the TEMPO radical itself cannot be observed due to the low molar absorption coefficient of TEMPO as compared to the PDI chromophores. However, the presence of the TEMPO substituent may have an influence on the solute-solvent interactions and induce a spectral shift of the absorption peaks. While no spectral shift is observed between PDI_{0sg} and PDI_{0sg}-TEMPO, the UV-vis absorption spectra of PDI_{4sg}-TEMPO and PDI_{4sg}-(TEMPO)₂ are slightly red-shifted as compared to that of PDI_{4sg}. While the absorption maximum is found at 571 nm for PDI_{4sg}, it is shifted to 575 nm for PDI_{4sg}-TEMPO and further on to 577 nm for PDI_{4sg}-(TEMPO)₂.

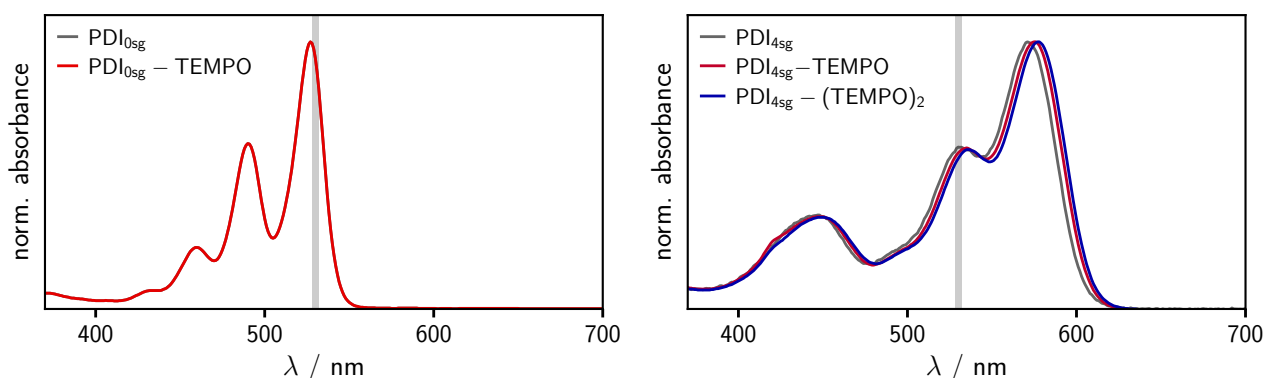


Figure S1: Comparison of the UV-vis absorption spectra measured for PDI_{0sg}-TEMPO (*left*) and PDI_{4sg}-TEMPO and PDI_{4sg}-(TEMPO)₂ (*right*) to the spectra of their parent chromophores without TEMPO. All data were acquired in toluene solution at room temperature. The gray vertical lines indicate the excitation wavelength of 530 nm.

2.2 Time-correlated single photon counting

The fluorescence lifetimes of the two PDI chromophores were determined by time-correlated single photon counting as detailed in the main part.

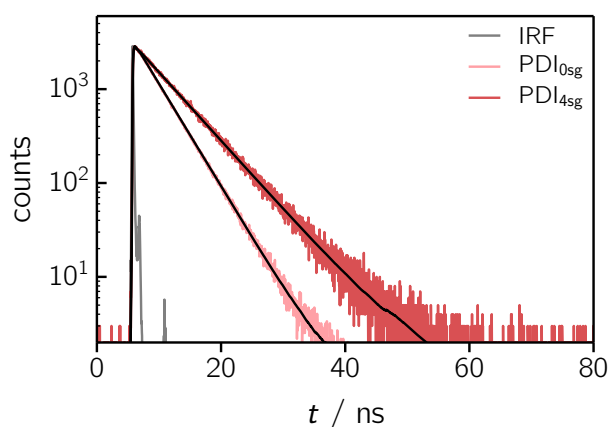


Figure S2: Time traces of the fluorescence decay measured for PDI_{0sg} and PDI_{4sg} by time-correlated single photon counting including the best monoexponential fits to the data.

Figure S2 shows the measured fluorescence decays together with a monoexponential fit, yielding fluorescence lifetimes of $\tau_F = 3.95$ ns for PDI_{0sg} and $\tau_F = 5.94$ ns for PDI_{4sg}. These time constants

for the decay of the excited singlet state were kept fixed in the analysis of the fsTA data of the PDI chromophores.

2.3 Calculation of the radiative rate constant using the Strickler-Berg equation

The radiative rate constant k_r^{SB} , as derived by Strickler and Berg [9] as well as Birks and Dyson [10], is given as

$$k_r^{\text{SB}} = \frac{8\pi c \ln(10)}{N_A} \frac{n_f^3}{n_i} \frac{g_f}{g_i} \cdot \frac{\int F(\tilde{\nu}) d\tilde{\nu}}{\int F(\tilde{\nu}) \tilde{\nu}^{-3} d\tilde{\nu}} \cdot \int \epsilon(\tilde{\nu}) \tilde{\nu}^{-1} d\tilde{\nu} \quad (\text{S1})$$

where c is the speed of light, N_A the Avogadro constant, ϵ the molar absorption coefficient and $F(\tilde{\nu})$ the corrected fluorescence signal as a function of wavenumber. The parameter g represents the vibronic degeneracy of the final and initial states. Since the spectral shift between the absorption and emission spectra is small, the dispersion of the refractive index n can be assumed to be negligible and $\frac{n_f^3}{n_i}$ can be replaced by n^2 . Assuming further that $g_f = g_i$, the radiative rate constants calculated for PDI_{0sg} and PDI_{4sg} amount to $k_r = 2.5 \cdot 10^8 \text{ s}^{-1}$ and $1.2 \cdot 10^8 \text{ s}^{-1}$, respectively. In these calculations, we used molar absorption coefficients of $7.1 \cdot 10^4 \text{ M}^{-1}\text{cm}^{-1}$ for PDI_{0sg} [11] and $3.1 \cdot 10^4 \text{ M}^{-1}\text{cm}^{-1}$ as determined for PDI_{4sg}.

Considering the measured fluorescence quantum yields of the two PDI chromophores and the definition of the fluorescence quantum yield

$$\Phi_F = \frac{N_{\text{emitted}}}{N_{\text{absorbed}}} = \frac{k_r}{k_r + k_{\text{IC}} + k_{\text{ISC}} + \dots} = k_r \cdot \tau_F \quad (\text{S2})$$

we obtain calculated fluorescence lifetimes of $\tau_F^{\text{SB}} = 3.9 \text{ ns}$ for PDI_{0sg} and 7.9 ns for PDI_{4sg}.

2.4 Calculation of the Förster energy transfer rate constant

Although the TEMPO radical absorbs only weakly in the visible range, we need to consider the possibility of Förster resonance energy transfer (FRET) between the PDI chromophores and the TEMPO radical. The molar absorption coefficient of the TEMPO radical is $\epsilon = 10.5 \text{ M}^{-1}\text{cm}^{-1}$ at its absorption maximum in the visible range of $\sim 470 \text{ nm}$ [14]. The fluorescence quantum yield of the PDI chromophores was measured on an absolute quantum yield spectrometer (cf. main text) and the center-to-center distance r_{DA} was taken from a DFT model of the PDI–TEMPO structures (vide infra).

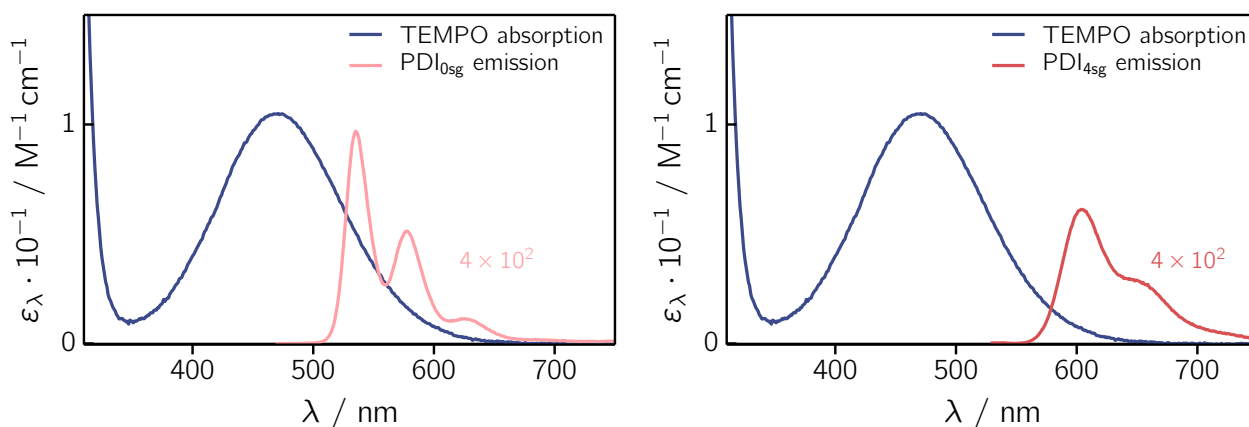


Figure S3: UV-vis absorption spectrum of the TEMPO radical and illustration of the spectral overlap of fluorescence emission and radical absorption for PDI_{0sg} (left) and PDI_{4sg} (right).

Table S1: Overview of the results from the calculation of the Förster radius, FRET time constants, and efficiencies for the two PDI–TEMPO structures. The following parameters were used: $r_{DA} = 0.99$ nm, $n = 1.496$ (toluene), $\tau_{F,0}^D = 4.0$ ns for PDI_{0sg} and 5.9 ns for PDI_{4sg}, $\Phi_{F,0}^D = 0.97$ for PDI_{0sg} and 0.92 for PDI_{4sg}, $\epsilon^A = 10.5 \text{ M}^{-1} \text{ cm}^{-1}$.

compound	κ^2	R_0 / nm	τ_{FRET} / ns	Φ_{FRET} / %
PDI _{0sg} –TEMPO	4 (collinear)	1.64	0.19	95.2
PDI _{0sg} –TEMPO	1 (parallel)	1.30	0.77	80.8
PDI _{0sg} –TEMPO	2/3 (random)	1.22	1.15	71.2
PDI _{4sg} –TEMPO	4 (collinear)	1.25	1.48	74.9
PDI _{4sg} –TEMPO	1 (parallel)	0.99	5.92	–
PDI _{4sg} –TEMPO	2/3 (random)	0.92	8.88	–

The Förster radius R_0 (obtained in nm) can be calculated from [15]

$$R_0^6 = 8.785 \cdot 10^{-11} \frac{\Phi_{F,0}^D \kappa^2}{n^4} \int I_F^D(\lambda) \epsilon^A(\lambda) \lambda^4 d\lambda \quad (\text{S3})$$

with

$$\int I_F^D(\lambda) d\lambda = 1 \quad (\text{S4})$$

where $\Phi_{F,0}^D$ and I_F^D are the fluorescence quantum yield and fluorescence intensity of the donor, ϵ^A is the molar absorption coefficient (in $\text{M}^{-1} \text{ cm}^{-1}$) of the acceptor and n the refractive index of the medium. The orientation factor κ^2 accounts for the relative orientation of the two transition dipole moment vectors (emission of donor and absorption of acceptor) with respect to the axis connecting the FRET pair.

The energy transfer rate constant and FRET efficiency are then given as

$$\tau_{\text{FRET}}^{-1} = k_{\text{FRET}} = \frac{1}{\tau_{F,0}^D} \left(\frac{R_0}{r_{DA}} \right)^6 \quad (\text{S5})$$

and

$$\Phi_{\text{FRET}} = 1 - \frac{\tau_{\text{FRET}}}{\tau_{F,0}^D} \quad (\text{S6})$$

where $\tau_{F,0}^D$ is the fluorescence lifetime of the donor in the absence of any quenchers and r_{DA} is the center-to-center distance (point dipole) between donor and acceptor. The results obtained for the two different PDI–TEMPO compounds, are summarized in Table S1.

3 Additional fsTA data and global kinetic analysis

3.1 TA data for the PDI_{4sg}-based compounds

Figure S4 shows contour plots of the fsTA data recorded for PDI_{4sg}, PDI_{4sg}-TEMPO, and PDI_{4sg}-(TEMPO)₂ in toluene at room temperature. The data for PDI_{4sg} and PDI_{4sg}-TEMPO were already shown, analyzed and discussed in reference [3]. Compared to PDI_{4sg}-TEMPO, the deactivation of the S₁ state is considerably enhanced in PDI_{4sg}-(TEMPO)₂.

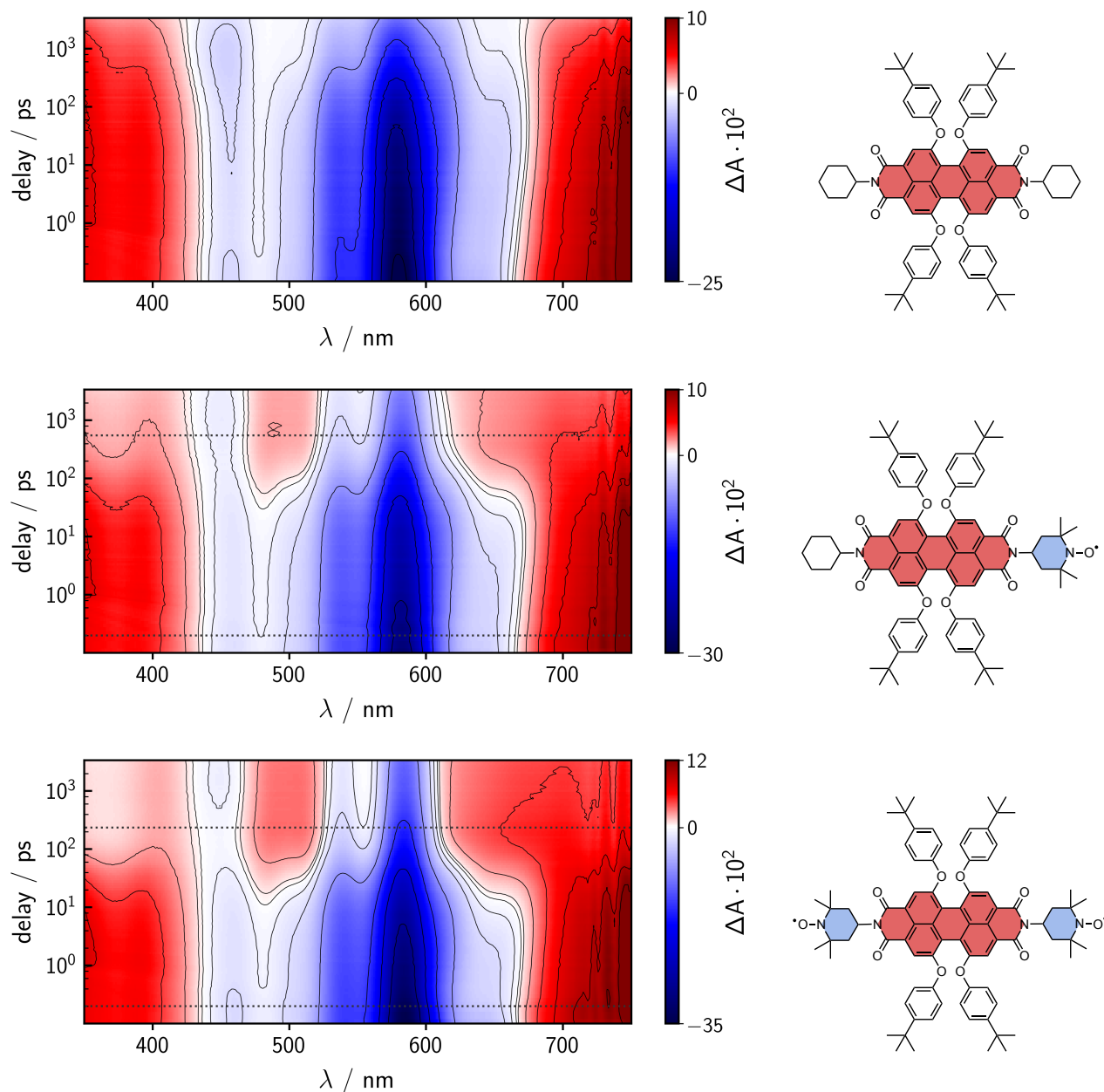


Figure S4: Contour plots of the fsTA data of PDI_{4sg} (*top*), PDI_{4sg}-TEMPO (*center*), and PDI_{4sg}-(TEMPO)₂ (*bottom*) recorded at room temperature in toluene. The horizontal dotted lines in the contour plots indicate the time points of 0.2 ps and $5 \times \tau_{S_1}$.

3.2 Global kinetic analysis

To determine the time constants of the excited state reaction processes, a global kinetic analysis of the recorded fsTA data was carried out. A multi-exponential function convoluted with the instrument

response function (IRF) served as the trial function. The procedure yields time constants and decay associated spectra (DAS). In all cases, it was found that three time constants were required to reproduce the experimental data satisfactorily.

The DAS obtained for the PDI–TEMPO compounds are shown in Figures S5 and S6.

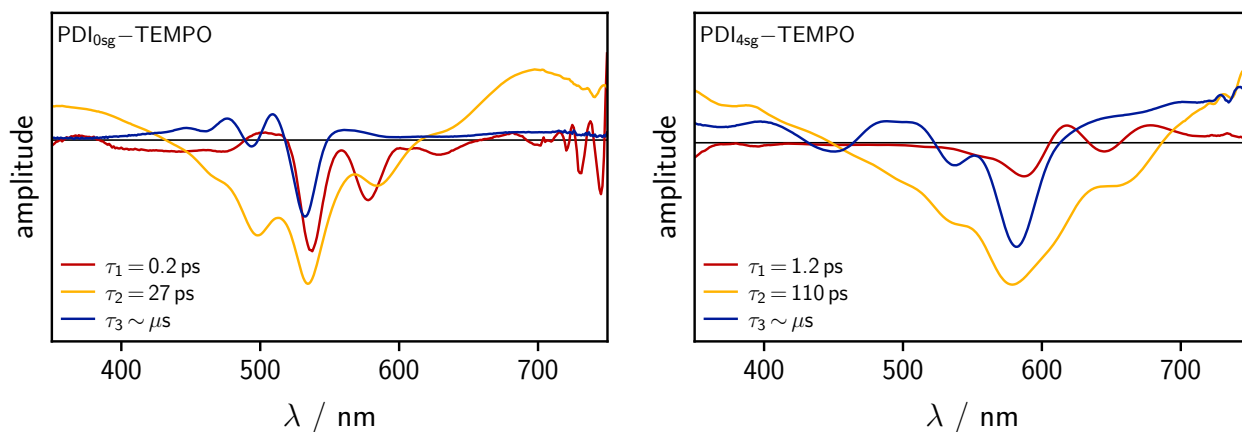


Figure S5: Decay associated spectra and time constants obtained from a global kinetic analysis of the femtosecond TA data of PDI_{0sg}–TEMPO (*left*) and PDI_{4sg}–TEMPO (*right*) in toluene. The triplet/quartet lifetime was fixed to 1 μ s.

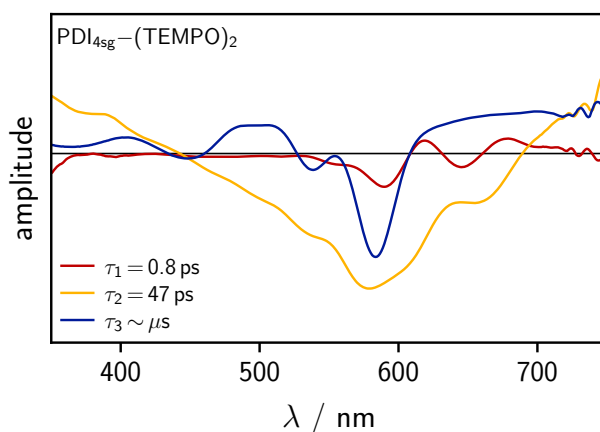


Figure S6: Decay associated spectra and time constants obtained from a global kinetic analysis of the femtosecond TA data of PDI_{4sg}–(TEMPO)₂ in toluene. The triplet/quintet lifetime was fixed to 1 μ s.

3.3 Triplet yield determination from the fsTA data

The EISC yields were determined by comparing the amplitude of the ground state bleach (GSB) directly after photoexcitation and a time corresponding to $5 \cdot \tau_{S1}$, as detailed in the main text ($\tau_{S1} = \tau_2$) and shown on the example of PDI_{0sg}–TEMPO in Figure S7. It can be seen that the contribution of stimulated emission (SE) to the ground state bleach amplitude near the intensity maximum of the steady-state absorption spectrum is significant at early times after photoexcitation, making it necessary to subtract this contribution from the data before calculating the triplet yield from the ground state bleach amplitudes. For the spectra measured at a time delay corresponding to $5 \cdot \tau_{S1}$, stimulated emission does not contribute to the spectral shape. As a consequence, the amplitude of the excited state absorption (ESA) in the range where the steady state absorption spectrum is zero (i.e. >560 nm) can be used as a reference for the scaling of the GSB amplitude.

In Figure S7, the contribution denoted 'GSB' shows the inverted and scaled UV-vis absorption spectrum of the compound, while 'SE' is the inverted and scaled fluorescence spectrum. The triplet yield was then calculated by dividing amplitude 2 by amplitude 1.

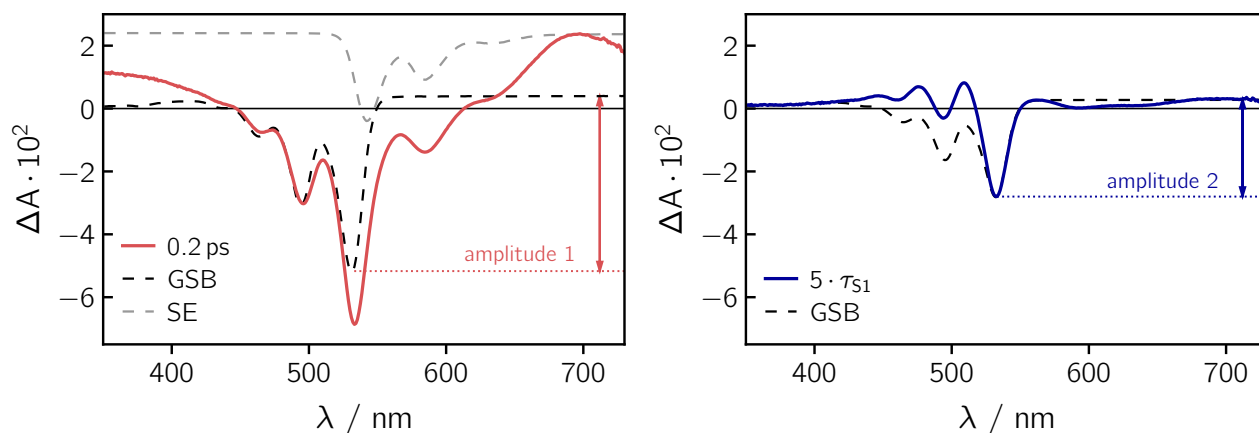


Figure S7: Calculation of the triplet yield from the amplitudes of the ground state bleach directly after photoexcitation (amplitude 1) and when triplet formation was considered complete ($5 \cdot \tau_{S1}$, amplitude 2). The contributions from stimulated emission and excited state absorption were taken into account.

Especially at early times after photoexcitation, when GSB and SE both contribute to the spectral shape and potentially overlap with ESA, there may be some ambiguity regarding the correct scaling of the ground state bleach amplitude. Although this ambiguity is somewhat alleviated in our case by the presence of very sharp absorption and emission features, we performed the analysis with different plausible scaling factors for all compounds to get an idea about the error on the resulting triplet yields. We estimate this error to be of the order of $\pm 5\%$. Table S2 gives an overview of the obtained time constants and EISC yields.

Table S2: Time constants and yields obtained from a global kinetic analysis of the fsTA data of $\text{PDI}_{0\text{sg}}-\text{TEMPO}$, $\text{PDI}_{4\text{sg}}-\text{TEMPO}$, and $\text{PDI}_{4\text{sg}}-(\text{TEMPO})_2$ in toluene solution at room temperature.

compound	τ_1 / ps	τ_2 / ps	τ_3 / ps	Φ_{EISC}
$\text{PDI}_{0\text{sg}}-\text{TEMPO}$	0.2	27	$> 10^6$	0.55
$\text{PDI}_{4\text{sg}}-\text{TEMPO}$	1.2	110	$> 10^6$	0.51
$\text{PDI}_{4\text{sg}}-(\text{TEMPO})_2$	0.8	47	$> 10^6$	0.57

3.4 Influence of the solvent

The room temperature femtosecond TA experiments were also carried out using 2-methyltetrahydrofuran as the solvent to explore the influence of the solvent polarity on the excited state reaction rate constants and yields.

Figure S8 shows the contour plots of the fsTA data obtained for the three PDI–TEMPO compounds in 2-methyltetrahydrofuran. Overall, it is observed that the spectral signatures are very similar, but the rate constants and triplet formation yields seem to be influenced by the solvent polarity.

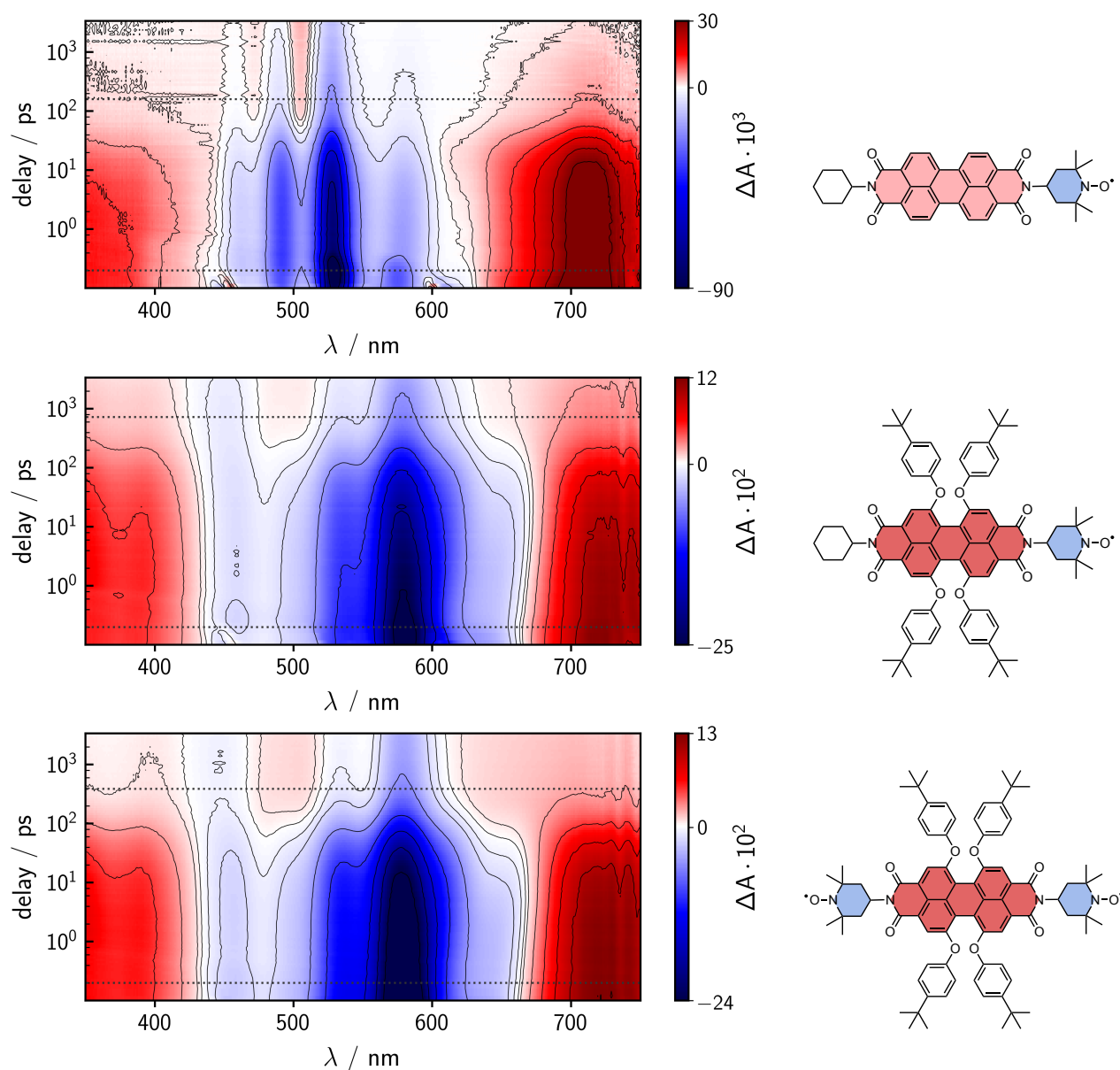


Figure S8: Contour plots of the fsTA data of PDI_{0sg}–TEMPO (*top*), PDI_{4sg}–TEMPO (*center*), and PDI_{4sg}–(TEMPO)₂ (*bottom*) recorded at room temperature in 2-methyltetrahydrofuran. The horizontal dotted lines in the contour plots indicate the time points of 0.2 ps and $5 \times \tau_{S1}$.

Figure S9 shows a comparison of the spectral shapes and kinetics obtained for PDI_{0sg}–TEMPO, PDI_{4sg}–TEMPO, and PDI_{4sg}–(TEMPO)₂ in 2-methyltetrahydrofuran solution at room temperature.

The fsTA data of the three PDI–TEMPO compounds in 2-methyltetrahydrofuran were subjected to a global kinetic analysis, using an analogous procedure as for the data in toluene. Table S3 summarizes the time constants obtained along with the EISC yields obtained from the analysis of the ground state

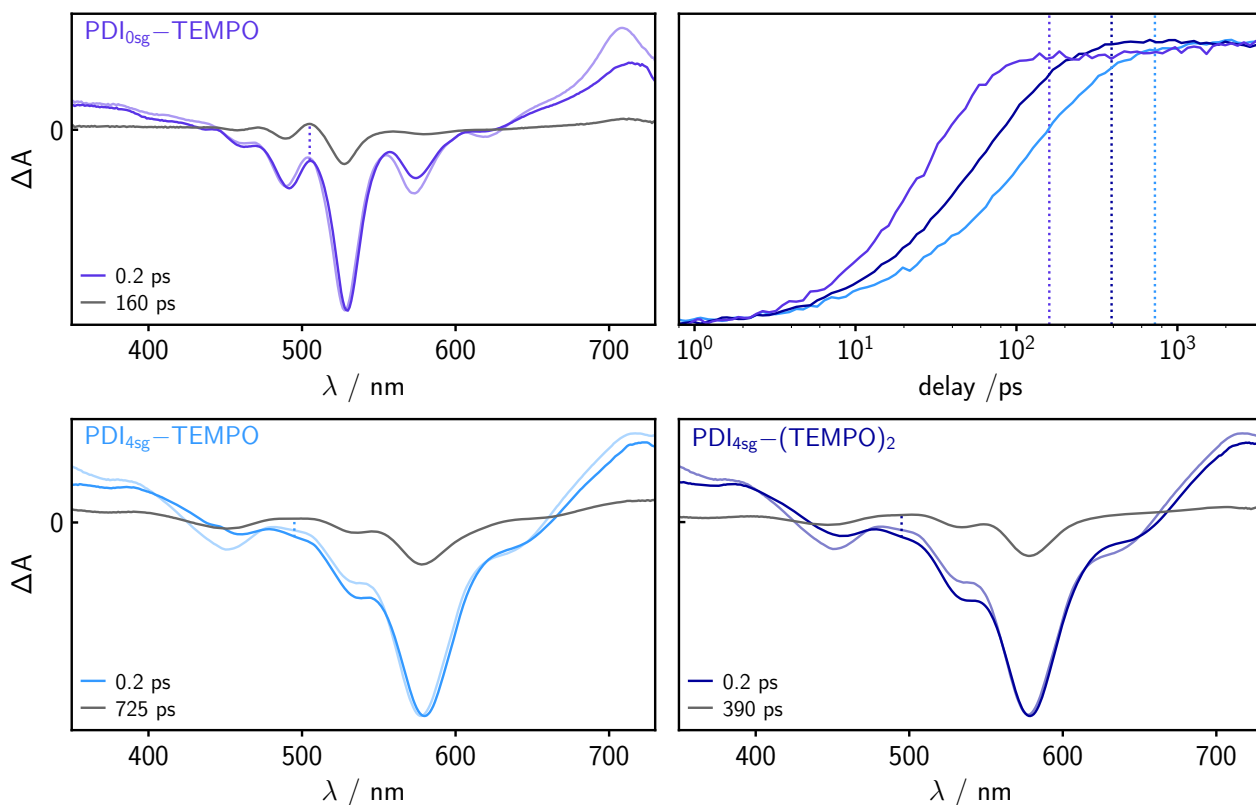


Figure S9: Comparison of the fsTA spectra and kinetics of PDI_{0sg}-TEMPO, PDI_{4sg}-TEMPO, and PDI_{4sg}-(TEMPO)₂ recorded in 2-methyltetrahydrofuran. The spectra are shown at 0.2 ps (colored line) and a time delay corresponding to $5 \times \tau_{S1}$ (gray line, delay as indicated). The vertical dotted lines in the spectra close to 500 nm indicate the wavelengths chosen for the visual comparison of the kinetics, while the colored vertical lines in the kinetic subplot indicate the time delays corresponding to the respective spectra taken at $5 \times \tau_{S1}$. For a comparison of the spectral shape, the spectrum measured for the parent chromophores (without TEMPO) in the same solvent is superimposed onto the spectra recorded at 0.2 ps (light colored trace).

bleach amplitudes. It can be seen that the S_1 state deactivation rate constant as well as the EISC yield is significantly decreased for all compounds in 2-methyltetrahydrofuran solution compared to toluene.

Table S3: Time constants and yields obtained from a global kinetic analysis of the fsTA data of PDI_{0sg}-TEMPO, PDI_{4sg}-TEMPO, and PDI_{4sg}-(TEMPO)₂ in 2-methyltetrahydrofuran solution at room temperature.

compound	τ_1 / ps	τ_2 / ps	τ_3 / ps	Φ_{EISC}
PDI _{0sg} -TEMPO	7.6	32	$> 10^6$	0.31
PDI _{4sg} -TEMPO	3.6	145	$> 10^6$	0.25
PDI _{4sg} -(TEMPO) ₂	3.5	78	$> 10^6$	0.21

The decay associated spectra obtained as a result of the global kinetic analysis are shown for all PDI-TEMPO compounds in Figures S10 and S11.

To demonstrate the absence of any PDI anion signatures in the fsTA data of PDI_{4sg}-TEMPO, additional spectra were recorded in both toluene and tetrahydrofuran using an extended spectral detection window [2, 3]. The spectra were compared to those of the parent chromophores without TEMPO where no electron transfer can occur. No marked differences in the spectral shapes are observed over the first ~ 100 – 200 ps until the shape of the spectrum of PDI_{4sg}-TEMPO changes due to triplet formation. The

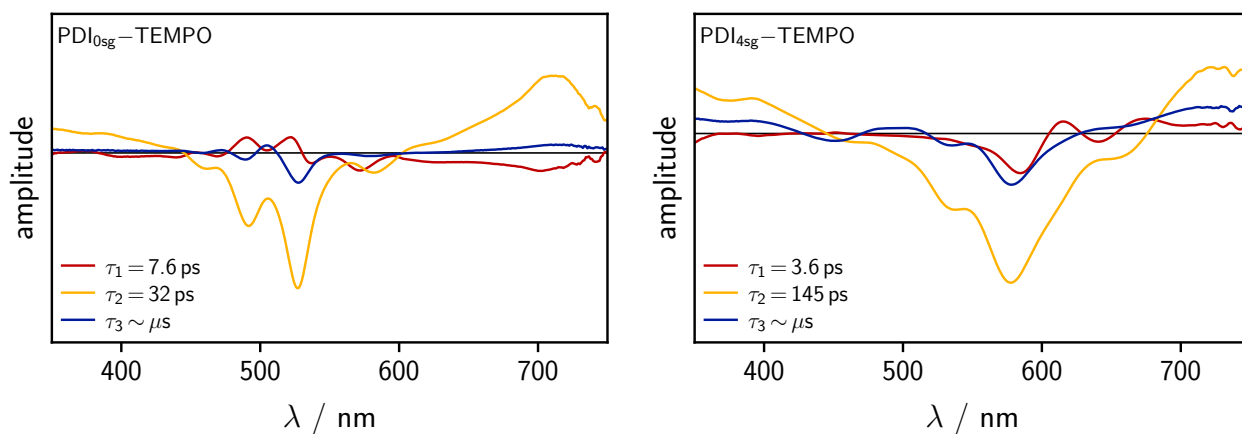


Figure S10: Decay associated spectra and time constants obtained from a global kinetic analysis of the femtosecond TA data of PDI_{0sg}-TEMPO (*left*) and PDI_{4sg}-TEMPO (*right*) in 2-methyltetrahydrofuran. The triplet/quartet lifetime was fixed to 1 μ s.

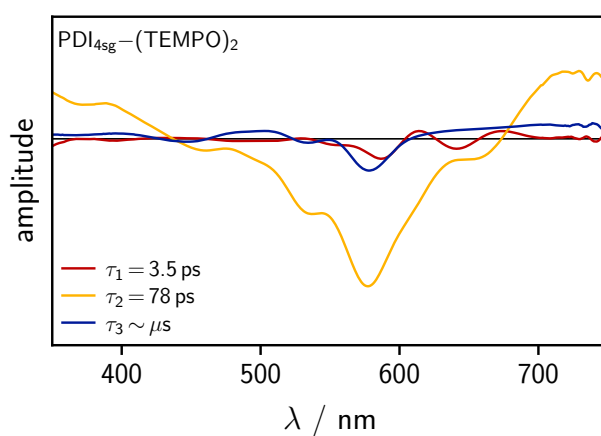


Figure S11: Decay associated spectra and time constants obtained from a global kinetic analysis of the femtosecond TA data of PDI_{4sg}-(TEMPO)₂ in 2-methyltetrahydrofuran. The triplet/quintet lifetime was fixed to 1 μ s.

spectra recorded at 1 ps after photoexcitation are compared in Figure S12.

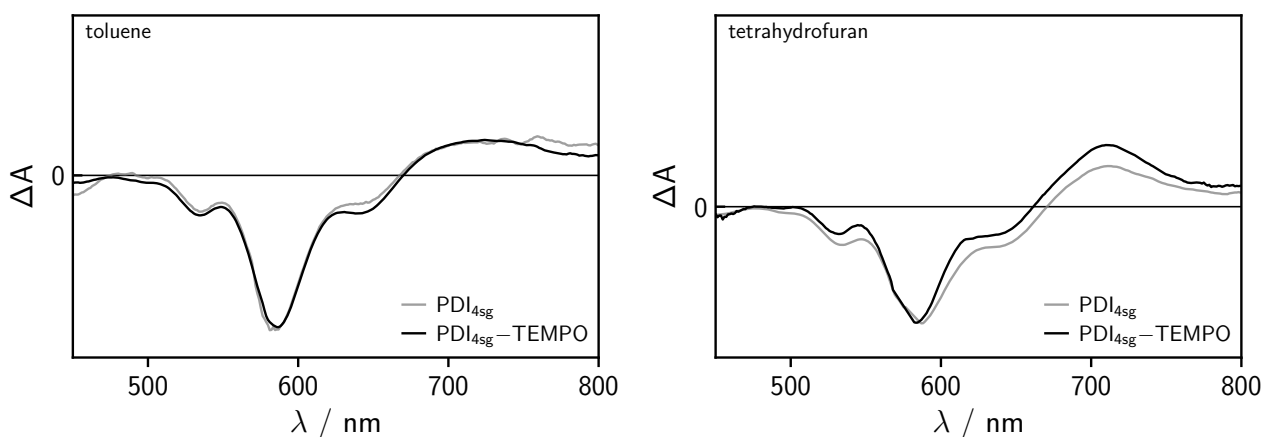


Figure S12: Comparison of the fsTA spectra of PDI_{4sg}-TEMPO in toluene (*left*) and tetrahydrofuran (*right*) with those of PDI_{4sg} recorded in the same solvent. The spectra are shown at 1 ps after photoexcitation. The measurements used an extended spectral detection window to confirm the absence of any signals at 780 nm indicative for PDI anion formation.

3.5 Calculation of the driving forces for electron transfer

The calculations of the driving forces $-\Delta G_0$ for charge separation (CS) and charge recombination (CR) were performed assuming the validity of the following equations [16]

$$-\Delta G_{0,CS} = -\Delta G_{0,IP} + E_{00} \quad (S7)$$

$$-\Delta G_{0,CR} = \Delta G_{0,IP} \quad (S8)$$

$$\Delta G_{0,IP} = e [E_{ox}(D) - E_{red}(A)] + C + S \quad (S9)$$

where the subscript IP stands for ion pair, E_{00} is the energy of the first excited singlet state and $E_{ox}(D)$ and $E_{red}(A)$ are the oxidation potentials of the electron donor and reduction potentials of the electron acceptor, respectively. The terms C and S represent the coulomb and solvent correction terms, defined as

$$C = -\frac{e^2}{4\pi\epsilon_0\epsilon_r r_{ee}} \quad S = \frac{e^2}{8\pi\epsilon_0} \left(\frac{1}{r_D} + \frac{1}{r_A} \right) \left(\frac{1}{\epsilon_r} - \frac{1}{\epsilon_{r,ref}} \right) \quad (S10)$$

where r_{ee} , ϵ_r , ϵ_0 , $\epsilon_{r,ref}$ and r_i are the edge-to-edge distance between the reaction partners, the relative solvent permittivity, the vacuum permittivity, the relative permittivity of the solvent used to determine the redox potentials and the Van-der-Waals radii, respectively.

The edge-to-edge distance for electron transfer, as well as the Van-der-Waals radii for donor (TEMPO) and acceptor (PDI) were assumed to be identical for all PDIs and taken from reference [17], where the following values were reported: $r_{ee} = 8.3 \text{ \AA}$, $r_D = 3.1 \text{ \AA}$, and $r_A = 6.3 \text{ \AA}$.

PDI chromophores with a core twist are generally found to be harder to reduce. The oxidation potential of TEMPO is 0.69 V vs. SCE [18], while the reduction potentials of the different PDI acceptors (vs. SCE) amount to -0.55 V [19], -0.61 V [20] and -0.67 V [2] for PDI_{0sg}, PDI_{2sg}, and PDI_{4sg}, respectively. The solvents were CHCl₃/acetonitrile, DMF, and CH₂Cl₂ with dielectric constants of ~ 21 (4.8 and 37.5), 37, and 9, respectively. Toluene has a relative dielectric constant of $\epsilon_r = 2.4$ at room temperature, whereas that of 2-methyltetrahydrofuran is $\epsilon_r = 7.0$ [21].

E_{00} is calculated from the crossing point of the absorption and fluorescence spectra and amounts to 2.33 eV (531 nm), 2.23 eV (556 nm), and 2.11 eV (588 nm) for PDI_{0sg}, PDI_{2sg}, and PDI_{4sg}, respectively.

Table S4: Calculated driving forces for charge separation (CS) and charge recombination (CR).

chromophore	toluene		2-methyltetrahydrofuran	
	$-\Delta G_{0,CS} / \text{eV}$	$-\Delta G_{0,CR} / \text{eV}$	$-\Delta G_{0,CS} / \text{eV}$	$-\Delta G_{0,CR} / \text{eV}$
PDI _{0sg}	0.53	1.80	1.06	1.27
PDI _{2sg}	0.30	1.93	0.83	1.40
PDI _{4sg}	0.41	1.70	0.94	1.17

The calculated driving forces for electron transfer $-\Delta G_0$ for charge separation and charge recombination between PDI and TEMPO are summarized in Table S4. Just by looking at the driving forces, one might assume that electron transfer is faster in 2-methyltetrahydrofuran as compared to toluene and equally feasible for PDI_{0sg} and PDI_{4sg} compared to PDI_{2sg}.

However, the actual rate constants for electron transfer will further depend on the corresponding

electronic matrix elements $|H_{AB}|^2$ and the reorganization energies λ . According to the classical Marcus theory for non-adiabatic electron transfer [22, 23]

$$k_{ET} = A \cdot \exp\left(-\frac{(\Delta G_0 + \lambda)^2}{4\lambda k_B T}\right) \quad (S11)$$

with

$$A = \frac{2\pi}{\hbar} |H_{AB}|^2 \cdot \frac{1}{\sqrt{4\pi\lambda k_B T}} \quad (S12)$$

where

$$\lambda = \lambda_{\text{inner}} + \lambda_{\text{outer}} \quad (S13)$$

and the inner and outer sphere contributions to the reorganization energy are given as

$$\lambda_{\text{inner}} = \frac{1}{2} \sum_i f_i (r_R^{\text{eq}} - r_P^{\text{eq}})^2 \quad (S14)$$

$$\lambda_{\text{outer}} = \frac{e^2}{4\pi\epsilon_0} \left(\frac{1}{2r_D} + \frac{1}{2r_A} - \frac{1}{r_{DA}} \right) \left(\frac{1}{n^2} - \frac{1}{\epsilon_r} \right) \quad (S15)$$

The outer sphere solvent reorganization energy can be calculated using the van-der-Waals radii listed above and amounts to 0.045 eV in toluene, while for 2-methyltetrahydrofuran a value of 0.627 eV is obtained.

For both TEMPO and a PDI chromophore without core substituents, literature values for the inner sphere reorganization energies are available: The inner sphere reorganization energy for the TEMPO \bullet /TEMPO $^+$ self-exchange process has been determined experimentally to amount to 0.347 eV [24], while, for an unsubstituted PDI chromophore, DFT calculations on the PDI/PDI $^+$ couple suggest $\lambda_{\text{inner}}^{\text{self}} = 0.262$ eV [25]. Considering that the electron transfer reaction can be split into two electron self-exchange processes [26], the total inner sphere reorganization energy $\lambda_{i, \text{total}} = \frac{1}{2}(\lambda_{i, D}^{\text{self}} + \lambda_{i, A}^{\text{self}})$ for the electron transfer between PDI and TEMPO can be estimated to ~ 0.305 eV based on the above values.

Regarding the inner and outer sphere reorganization energies, no major differences are expected between the three different PDI chromophores. The total reorganization energy ($\lambda_{\text{inner}} + \lambda_{\text{outer}}$) can thus be estimated to amount to about 0.35 eV in toluene and 0.93 eV in 2-methyltetrahydrofuran. Considering the above values for the driving forces for charge separation and the reorganization energies, one notices that $-\Delta G_0$ and λ have very similar magnitudes in both solvents, indicating that the electron transfer reaction should proceed almost barrierless and be equally feasible in both solvents: The higher outer reorganization energy in 2-methyltetrahydrofuran is largely compensated by the higher driving force $-\Delta G_0$ resulting in a similar result for the reorganization- and driving force-dependent terms in the expression for the electron transfer rate constant: $\frac{1}{\sqrt{4\pi\lambda k_B T}} \cdot \exp\left(-\frac{(\Delta G_0 + \lambda)^2}{4\lambda k_B T}\right)$.

Considering charge recombination to the chromophore triplet state (i.e. inverted kinetics), as discussed in the main part, the driving forces for charge recombination, $-\Delta G_{0, CR}$, can be calculated taking into account the vertical triplet energies computed by TD-DFT (*vide infra*). In toluene, $-\Delta G_{0, CR}$ amounts to 0.35, 0.53, and 0.38 eV for PDI $_{0sg}$ -TEMPO, PDI $_{2sg}$ -TEMPO, and PDI $_{4sg}$ -TEMPO, respectively. In 2-methyltetrahydrofuran, $-\Delta G_{0, CR}$ calculated for recombination to the triplet state is close to zero for all PDI-TEMPO compounds, however, it needs to be considered that the actual triplet energies are likely to be lower than the vertical energies computed by TD-DFT which suggests a slightly positive value for $-\Delta G_{0, CR}$.

4 Additional EPR data

4.1 Quantitative EPR on PDI_{4sg}-TEMPO and PDI_{4sg}-(TEMPO)₂

Solutions of PDI_{4sg}-TEMPO and PDI_{4sg}-(TEMPO)₂ in toluene with matched UV-vis absorbances (same concentration of PDI) were prepared to verify the presence of two TEMPO moieties per PDI unit in PDI_{4sg}-(TEMPO)₂. A modulation amplitude of 3 G and a microwave attenuation of 14 dB (100 mW source) were chosen for the continuous wave EPR experiments at room temperature on a Bruker EMXnano bench-top spectrometer with an integrated spin counting option. The spectra were baseline corrected, doubly integrated and then subjected to a quantitative EPR analysis, considering the sample volume (tube diameter, fill height), resonator geometry, and quality factor of the cavity. For both compounds, the obtained number of spins was roughly consistent with the expectations based on the PDI concentration estimated from the UV-vis absorbances. Importantly, the corrected spectra showed a roughly two-fold signal increase for PDI_{4sg}-(TEMPO)₂ as compared to PDI_{4sg}-TEMPO (see Figure S13), confirming the presence of two TEMPO radicals per PDI unit.

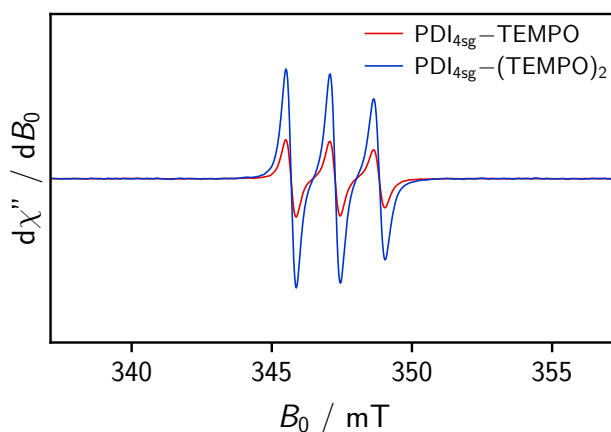


Figure S13: Comparison of the continuous wave EPR signal intensities obtained for PDI_{4sg}-TEMPO and PDI_{4sg}-(TEMPO)₂ in toluene solution at room temperature. The spectra were recorded using identical settings and sample concentrations. Slight differences in the quality factor of the cavity were also accounted for.

4.2 Transient nutation data for PDI_{4sg}-(TEMPO)₂

Figure S14 shows the frequency map obtained for PDI_{4sg}-(TEMPO)₂ in toluene after Fourier transform when measuring transient nutations as a function of the static magnetic field B_0 . The corresponding field-swept echo-detected EPR spectrum is shown above the nutation data for reference. It can be seen that the majority of the light-induced signal detected at 80 K can be attributed to a quartet state, while quintet signatures are also present indicating strong coupling between the chromophore triplet and the stable TEMPO radicals.

4.3 Double electron-electron resonance experiments on PDI_{4sg}-(TEMPO)₂

In order to confirm the distance between the two nitroxide radicals in PDI_{4sg}-(TEMPO)₂ and demonstrate the absence of any significant exchange coupling between them, double electron-electron resonance (DEER) experiments were carried out on PDI_{4sg}-(TEMPO)₂ in the dark. The four-pulse DEER experiments were performed at 80 K at the Q-band on a Bruker ELEXSYS E580 spectrom-

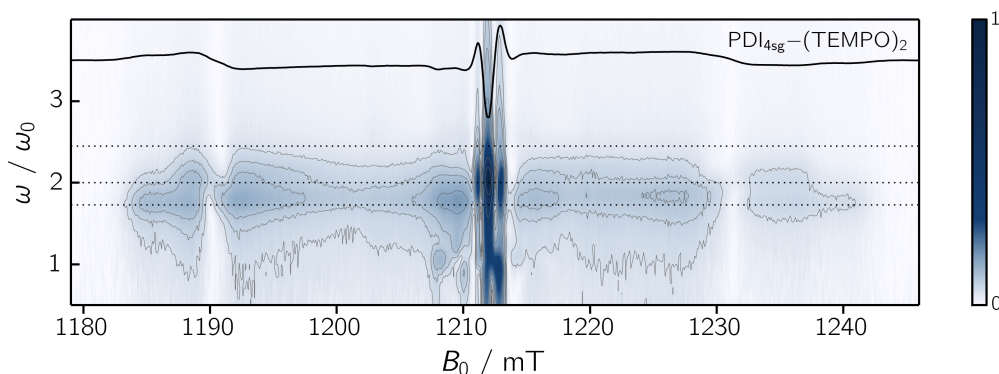


Figure S14: Transient nutation data as a function of magnetic field measured at the Q-band for $\text{PDI}_{4\text{sg}}-(\text{TEMPO})_2$ at $\text{DAF} = 9 \mu\text{s}$. The nutation frequency was normalized by that obtained for the TEMPO radical in the dark. The spectrum shown above the data corresponds to the light-induced signal measured at the same DAF.

ter equipped with a Bruker EN 5107D2 resonator and liquid nitrogen flow cryostat using the sequence $\frac{\pi}{2} - \tau_1 - \pi - \tau_1 - \tau_2 - \pi - \tau_2$ -echo at the detection frequency ν_{det} while applying a single π pulse at the pump frequency ν_{pump} during the interval $\tau_1 - \tau_2$. The pump π pulse position was varied step-wise starting at a time $t_0 < \tau_1$ after the first detection π pulse up to a time $t < \tau_1 + \tau_2$, shortly before the second π pulse at ν_{det} .

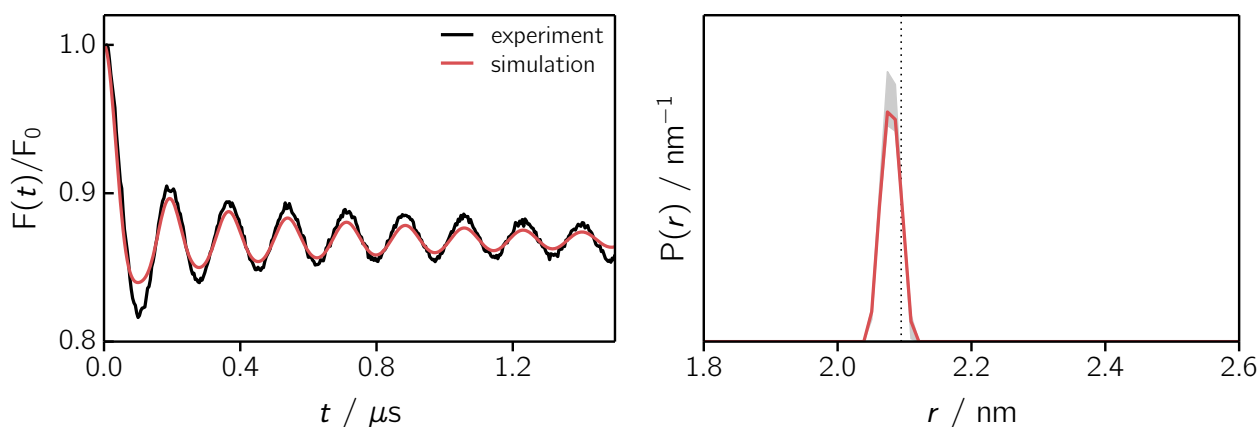


Figure S15: Experimental DEER trace for $\text{PDI}_{4\text{sg}}-(\text{TEMPO})_2$ (*left*) together with the corresponding fit obtained as a result from a model-free analysis employing Tikhonov regularization as implemented in DeerAnalysis and corresponding distance distribution (*right*). The black dotted line in the distance distribution indicates the distance obtained from DFT, measured roughly at the center of the predicted spin density distribution (center of the bond between N and O atoms of the nitroxide).

A pulse length of 32 ns was chosen for the pump pulse, whereas the detection $\frac{\pi}{2}$ and π pulses had lengths of 18 and 36 ns, respectively. The time intervals τ_1 and τ_2 had lengths of 140 ns and 2000 ns. A two-step phase cycle was applied on the first observer pulse to remove unwanted echos (incoherent ELDOR source). The pump frequency was set to the maximum of the field-swept echo-detected EPR spectrum of TEMPO and the detection frequency was $\nu_{\text{det}} = \nu_{\text{pump}} - 35 \text{ MHz}$. The positions of the pump and detection pulses in the resonator were symmetric with respect to the resonator dip and the pump pulse position was varied in steps of 4 ns. The data were collected at a repetition rate of 1000 μs .

The experimental DEER data were then phase-corrected and background-corrected using an exponential background function with a dimensionality of $d = 3$. To obtain the distance distribution shown in Figure S15, the corrected data were analysed in DeerAnalysis [27, 28]. Tikhonov regularization was

used to obtain the distance distribution and the regularization parameter α was set based on the L-curve criterion. A validation procedure was employed to verify the robustness of the solution and the obtained bounds are shown in gray in Figure S15 (*right*). The obtained distance distribution is centered at 2.08 nm, in good agreement with the predictions based on a DFT model of the structure (2.10 nm).

5 DFT calculations

5.1 TD-DFT calculations

To investigate the effect of the side groups on the transition energy (HOMO–LUMO gap) as well as on the energies of the excited singlet and triplet states, TD-DFT calculations were carried out on optimized structures of PDI_{0sg} and PDI_{4sg}. The geometry optimizations and HOMO/LUMO energies were computed at the B3LYP/def2-TZVP level of theory. On the optimized structures, single point TD-DFT calculations were performed using the same functional and basis set. A preoptimization of the structures (B3LYP/def2-SVP) was carried out using Gaussian [29], while all further calculations were performed using ORCA (version 4.2) [30].

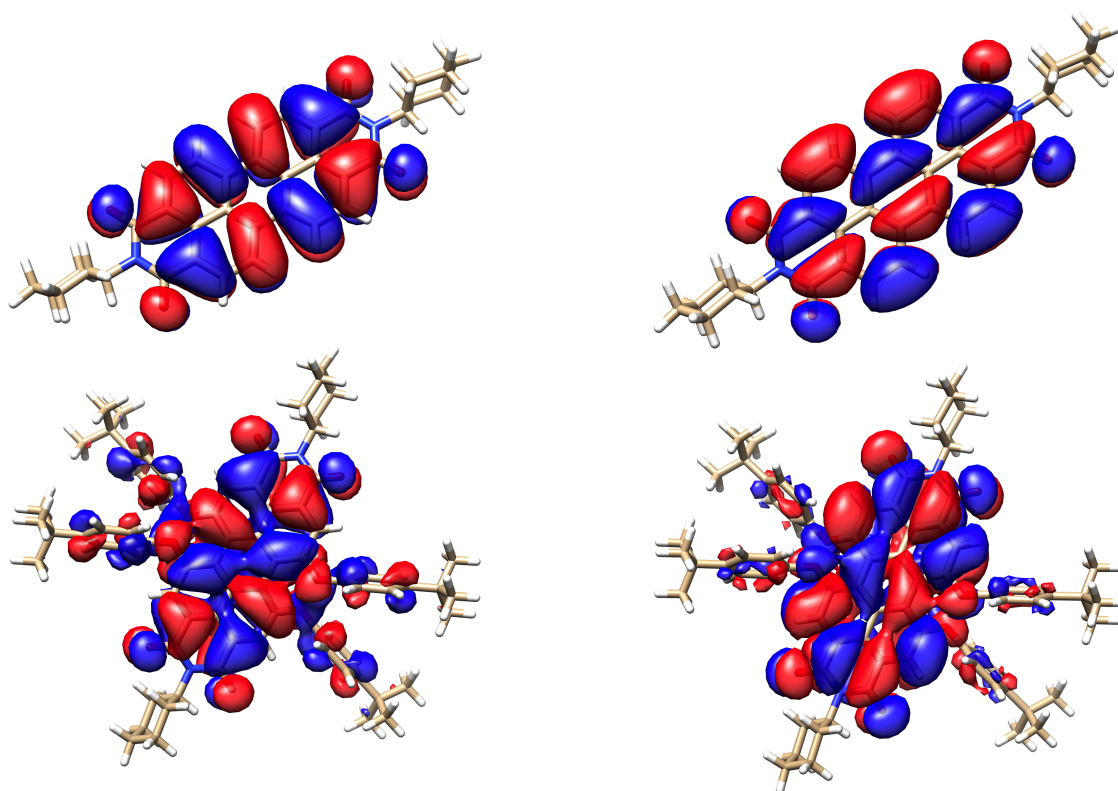


Figure S16: Visualization of the HOMO (*left*) and LUMO (*right*) orbitals of PDI_{0sg} (*top*) and PDI_{4sg} (*bottom*) calculated by DFT.

The HOMO and LUMO orbitals of PDI_{0sg} and PDI_{4sg} are shown in Figure S16. It is found that the HOMO and LUMO energies increase by ~ 0.75 eV and ~ 0.5 eV, respectively, when going from PDI_{0sg} to PDI_{4sg}. The calculated energies are generally too high with respect to measured experimental values [31], but the trend is predicted correctly. Regarding the HOMO–LUMO transition energies, DFT predicts a decrease in the HOMO–LUMO gap from 2.52 eV (492 nm) to 2.29 eV (541 nm).

The energies of the first excited singlet state are predicted as 2.609 eV and 2.271 eV, for PDI_{0sg} to PDI_{4sg}, respectively, corresponding to a spectral red-shift from 475 nm to 546 nm. This is in good

agreement with the experimentally observed red-shift of the UV-vis absorption maximum from 527 nm to 571 nm.

Considering vertical excitations as computed by DFT, the first excited singlet state is predicted to be almost isoenergetic with the second excited triplet state (T_2). The first three calculated triplet state energies are 1.448, 2.805, 2.897 eV and 1.319, 2.307, 2.342 eV, for PDI_{0sg} and PDI_{4sg}, respectively. For PDI_{0sg}, the first excited triplet state T_1 lies 1.16 eV below S_1 , while T_2 is predicted to be 0.20 eV above S_1 . For PDI_{4sg}, T_1 lies 0.95 eV below S_1 , while T_2 is predicted to be 0.036 eV above S_1 . At room temperature $k_B T = 0.025$ eV, so the second excited triplet state could be accessible.

In general it is observed that the energy gaps between the excited singlet and triplet states decrease when going from PDI_{0sg} to PDI_{2sg} and further on to PDI_{4sg}, which should favor the efficiency of EISC. For PDI_{2sg}, the calculated HOMO–LUMO gap is 2.42 eV, the calculated S_1 transition energy 2.462 eV (504 nm), and the first three triplet state energies are 1.404, 2.573, and 2.611 eV. Consequently, T_1 lies 1.06 eV below S_1 , while T_2 is predicted to be 0.11 eV above S_1 .

5.2 Calculation of the magnetic properties

The DFT calculations of the magnetic parameters were performed using the ORCA program package (version 4.0) [30]. For the calculation of the spin densities, the structures were first optimized in their overall doublet, triplet, quartet or quintet spin states using the B3LYP functional in combination with the def2-TZVP basis set and RI approximation. Magnetic property calculations used the B3LYP functional in combination with the EPR-II basis set.

A visual representation of the optimized molecular structures and calculated spin densities (iso values of 0.001) for the triplet states of the PDI chromophores as well as the doublet/triplet and quartet/quintet spin states of the corresponding PDI–TEMPO systems are shown in Figures S17 to S19.

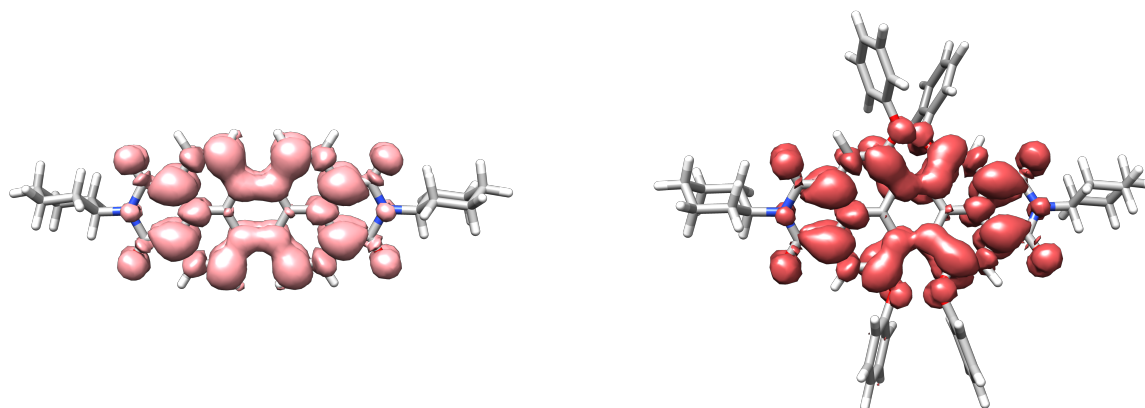


Figure S17: Visualization of the molecular structures and spin densities of the excited triplet states of PDI_{0sg} (*left*) and PDI_{4sg} (*right*) as predicted by DFT calculations.

Tables S5 and S6 give an overview of the calculated g and D values (where applicable) for the triplet states of the PDIs and the doublet/triplet and quartet/quintet spin states of the corresponding PDI–TEMPO compounds. The calculated isotropic nitrogen hyperfine couplings of the nitroxide moiety in the different spin states are also shown. While it is known that the magnitudes of the calculated magnetic properties can deviate substantially from the experimental ones (especially considering the D values), the trends are typically predicted correctly [32].

The D values of the PDI triplet states are predicted to be roughly twice as large compared to D_Q , meaning that the spectra of the triplet and quartet states are expected to have a similar width, especially

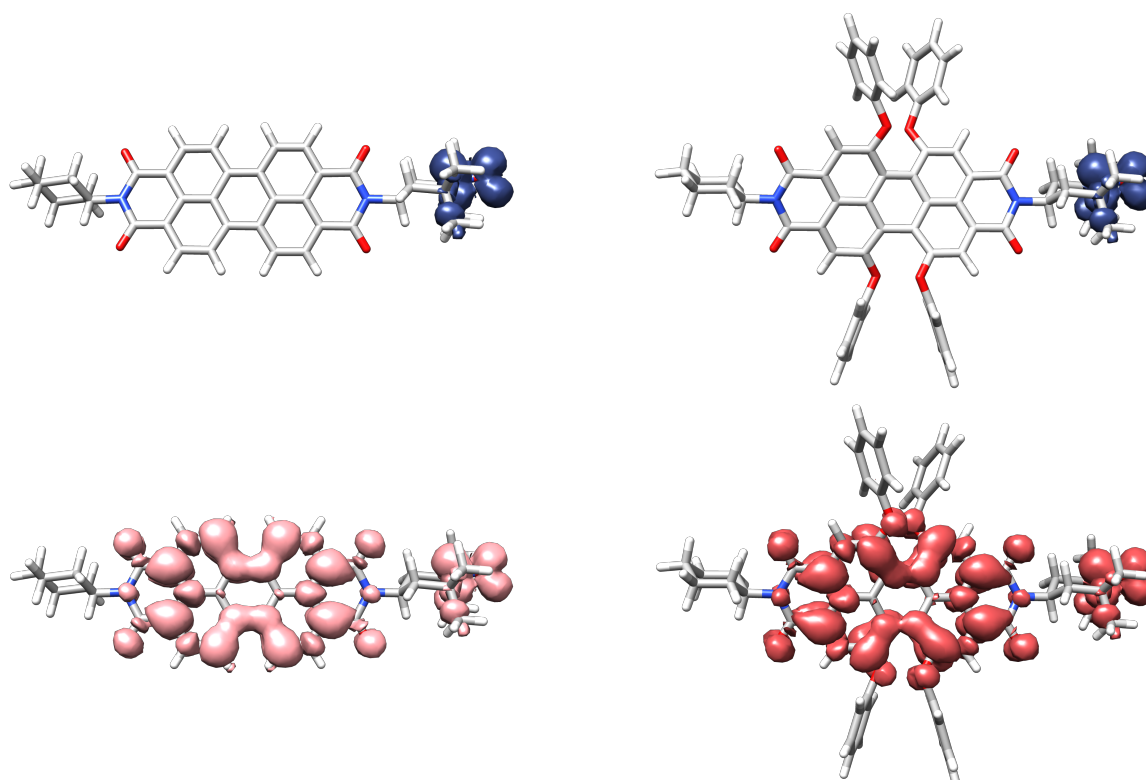


Figure S18: Visualization of the spin densities of the doublet (*top*) and trip-quartet (*bottom*) states of $\text{PDI}_{0\text{sg}}\text{-TEMPO}$ (*left*) and $\text{PDI}_{4\text{sg}}\text{-TEMPO}$ (*right*) as predicted by DFT calculations.

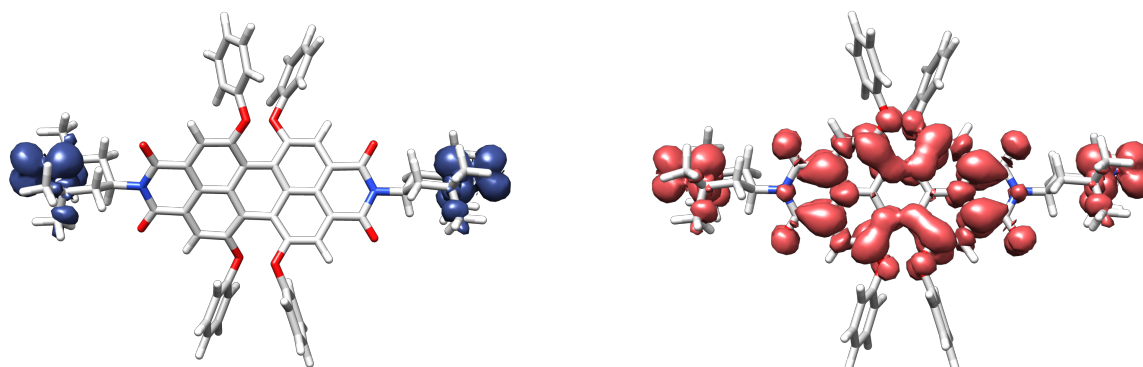


Figure S19: Visualization of the spin densities of the triplet (*left*) and quintet (*right*) states of $\text{PDI}_{4\text{sg}}\text{-(TEMPO)}_2$.

for the case of $\text{PDI}_{4\text{sg}}\text{-TEMPO}$. Compared to $\text{PDI}_{4\text{sg}}$, the triplet spectrum of $\text{PDI}_{0\text{sg}}$ is expected to be larger by a factor of 1.3, due to an increased localization of the triplet state wavefunction in the absence of the four side groups on the PDI core. A similar trend is predicted for the quartet states of $\text{PDI}_{0\text{sg}}\text{-TEMPO}$ and $\text{PDI}_{4\text{sg}}\text{-TEMPO}$. Compared to the quartet state of $\text{PDI}_{4\text{sg}}\text{-TEMPO}$, the D value of the quintet state of $\text{PDI}_{4\text{sg}}\text{-(TEMPO)}_2$ is reduced (cf. Table S6), but the spectral width of the EPR quartet and quintet spectra is expected to be similar, since, according to calculations, $4|D_{\text{Q}}| \simeq 6|D_{\text{Qu}}|$.

Table S5: Overview of the calculated isotropic g values for the triplet states of the PDIs and doublet/triplet and quartet/quintet spin states of the corresponding PDI–TEMPO compounds.

Compound	g_T	$g_{iso, D}$	g_Q	$g_{iso, Qu}$
PDI _{0sg}	2.0035	–	–	–
PDI _{0sg} –TEMPO	–	2.0068	2.0046	–
PDI _{4sg}	2.0038	–	–	–
PDI _{4sg} –TEMPO	–	2.0069	2.0048	–
PDI _{4sg} –(TEMPO) ₂	2.0070	–	–	2.0054

Table S6: Overview of the calculated D values for the triplet states of the PDIs and quartet/quintet states of the corresponding PDI–TEMPO compounds as well as the nitrogen hyperfine couplings (of the nitroxide) in the doublet/triplet and quartet/quintet states of the PDI–TEMPO compounds.

Compound	D_T / MHz	D_Q / MHz	D_{Qu} / MHz	$A_{iso, D}^N$ / MHz	$A_{iso, Q}^N$ / MHz	$A_{iso, Qu}^N$ / MHz
PDI _{0sg}	+600	–	–	–	–	–
PDI _{0sg} –TEMPO	–	–247	–	35.5	11.8	–
PDI _{4sg}	+464	–	–	–	–	–
PDI _{4sg} –TEMPO	–	–221	–	35.4	11.8	–
PDI _{4sg} –(TEMPO) ₂	–8.4	–	–143	–	–	8.6

References

- [1] Berberich, M.; Natali, M.; Spent, P.; Chiorboli, C.; Scandola, F.; Würthner, F. Nondestructive photoluminescence read-out by intramolecular electron transfer in a perylene bisimide-diarylethene dyad. *Chem. Eur. J.* **2012**, *18*, 13651–13664.
- [2] Wu, Y.; Young, R. M.; Frascioni, M.; Schneebeli, S. T.; Spent, P.; Gardner, D. M.; Brown, K. E.; Würthner, F.; Stoddart, J. F.; Wasielewski, M. R. Ultrafast photoinduced symmetry-breaking charge separation and electron sharing in perylenediimide molecular triangles. *J. Am. Chem. Soc.* **2015**, *137*, 13236–13239.
- [3] Mayländer, M.; Chen, S.; Lorenzo, E. R.; Wasielewski, M. R.; Richert, S. Exploring photogenerated molecular quartet states as spin qubits and qudits. *J. Am. Chem. Soc.* **2021**, *143*, 7050–7058.
- [4] Rademacher, A.; Maerke, S.; Langhals, H. Soluble perylene fluorescent dyes with high photostability. *Chem. Ber.* **1982**, *115*, 2927–2934.
- [5] Quante, H.; Schlichting, P.; Rohr, U.; Geerts, Y.; Müllen, K. Novel perylene-containing polymers. *Macromol. Chem. Phys.* **1996**, *197*, 4029–4044.
- [6] Kantarod, K.; Worakul, T.; Soorukam, D.; Kuhakarn, C.; Reutrakul, V.; Surawatanawong, P.; Wattanathana, W.; Leowanawat, P. Dibenzopleiadiene-embedded polyaromatics via [4+3] annulative decarbonylation/decarboxylation. *Org. Chem. Front.* **2021**, *8*, 522–530.
- [7] Wong, C. K.; Mason, A. F.; Stenzel, M. H.; Thordarson, P. Formation of non-spherical polymersomes driven by hydrophobic directional aromatic perylene interactions. *Nat. Commun.* **2017**, *8*, 1240.
- [8] Wang, R.; Shi, Z.; Zhang, C.; A., Z.; J., C.; Guo, W.; Z., S. Facile synthesis and controllable bromination of asymmetrical intermediates of perylene monoanhydride/monoimide diester. *Dyes Pigm.* **2013**, *98*, 450–458.
- [9] Strickler, S. J.; Berg, R. A. Relationship between absorption intensity and fluorescence lifetime of molecules. *J. Chem. Phys.* **1962**, *37*, 814–822.
- [10] Birks, J. B.; Dyson, D. J.; Flowers, B. H. The relations between the fluorescence and absorption properties of organic molecules. *Proc. R. Soc. Lond. A Math. Phys. Sci.* **1963**, *275*, 135–148.
- [11] Prathapan, S.; Yang, S. I.; Seth, J.; Miller, M. A.; Bocian, D. F.; Holten, D.; Lindsey, J. S. Synthesis and excited-state photodynamics of perylene–porphyrin dyads. 1. Parallel energy and charge transfer via a diphenylethyne linker. *J. Phys. Chem. B* **2001**, *105*, 8237–8248.
- [12] Feng, J.; Zhang, Y.; Zhao, C.; Li, R.; Xu, W.; Li, X.; Jiang, J. Cyclophanes of perylene tetracarboxylic diimide with different substituents at bay positions. *Org. Biomol. Chem.* **2011**, *9*, 8246–8252.
- [13] Würthner, F. Perylene bisimide dyes as versatile building blocks for functional supramolecular architectures. *Chem. Commun.* **2004**, 1564–1579.
- [14] Chateaufneuf, J.; Luszyk, J.; Ingold, K. U. Photoinduced electron transfer from dialkyl nitroxides to halogenated solvents. *J. Org. Chem.* **1990**, *55*, 1061–1065.
- [15] Lakowicz, J. R. *Principles of fluorescence spectroscopy*; Springer: New York, 2006.
- [16] Weller, A. Photoinduced electron transfer in solution: exciplex and radical ion pair formation free enthalpies and their solvent dependence. *Z. Phys. Chem.* **1982**, *133*, 93–98.
- [17] Colvin, M. T.; Giacobbe, E. M.; Cohen, B.; Miura, T.; Scott, A. M.; Wasielewski, M. R. Competitive electron transfer and enhanced intersystem crossing in photoexcited covalent TEMPO-peryene-3,4:9,10-bis(dicarboximide) dyads: Unusual spin polarization resulting from the radical-triplet interaction. *J. Phys. Chem. A* **2010**, *114*, 1741–1748.
- [18] Suga, T.; Pu, Y.-J.; Oyaizu, K.; Nishide, H. Electron-transfer kinetics of nitroxide radicals as an electrode-active material. *Bull. Chem. Soc. Jpn.* **2004**, *77*, 2203–2204.
- [19] Lee, S. K.; Zu, Y.; Herrmann, A.; Geerts, Y.; Müllen, K.; Bard, A. J. Electrochemistry, spectroscopy and electrogenerated chemiluminescence of perylene, terylene, and quaterylene diimides in aprotic solution. *J. Am. Chem. Soc.* **1999**, *121*, 3513–3520.

- [20] Van der Boom, T.; Hayes, R. T.; Zhao, Y.; Bushard, P. J.; Weiss, E. A.; Wasielewski, M. R. Charge transport in photofunctional nanoparticles self-assembled from zinc 5,10,15,20-tetrakis(perylene-diimide)porphyrin building blocks. *J. Am. Chem. Soc.* **2002**, *124*, 9582–9590.
- [21] Wohlfarth, C. In *Landolt-Börnstein, New Series*; Lechner, M. D., Ed.; Springer: Berlin, 2008.
- [22] Marcus, R. A.; Sutin, N. Electron transfers in chemistry and biology. *Biochim. Biophys. Acta* **1985**, *811*, 265–322.
- [23] Barbara, P. F.; Meyer, T. J.; Ratner, M. A. Contemporary Issues in Electron Transfer Research. *J. Phys. Chem.* **1996**, *100*, 13148–13168.
- [24] Grampp, G.; Rasmussen, K. Solvent dynamical effects on the electron self-exchange rate of the TEMPO•/TEMPO⁺ couple (TEMPO = 2,2,6,6-tetramethyl-1-piperidinyloxy radical). *Phys. Chem. Chem. Phys.* **2002**, *4*, 5546–5549.
- [25] Shoaib, M.; Ur-Rehman, S.; Shamsa, B.; Ullah, I.; Jamil, S.; Iqbal, J.; Alam, A.; Saeed, U.; Fu Quan, B. Theoretical investigation of perylene diimide derivatives as acceptors to match with benzodithiophene based donors for organic photovoltaic devices. *Z. Phys. Chem.* **2019**, *235*, 427–449.
- [26] López-Estrada, O.; Laguna, H. G.; Barrueta-Flores, C.; Amador-Bedolla, C. Reassessment of the four-point approach to the electron-transfer Marcus-Hush theory. *ACS Omega* **2018**, *3*, 2130–2140.
- [27] Jeschke, G.; Chechik, V.; Ionita, P.; Godt, A.; Zimmermann, H.; Banham, J.; Timmel, C. R.; Hilger, D.; Jung, H. DeerAnalysis2006 – a comprehensive software package for analyzing pulsed ELDOR data. *Appl. Magn. Reson.* **2006**, *30*, 473–498.
- [28] Fábregas Ibáñez, L.; Jeschke, G.; Stoll, S. DeerLab: a comprehensive software package for analyzing dipolar electron paramagnetic resonance spectroscopy data. *Magn. Reson.* **2020**, *1*, 209–224.
- [29] Frisch, M. J. et al. Gaussian 16 Revision C.01. 2016; Gaussian Inc. Wallingford CT.
- [30] Neese, F. Software update: the ORCA program system, version 4.0. *Wiley Interdiscip. Rev.: Comput. Mol. Sci.* **2017**, *8*, e1327.
- [31] Nowak-Król, A.; Shoyama, K.; Stolte, M.; Würthner, F. Naphthalene and perylene diimides – better alternatives to fullerenes for organic electronics? *Chem. Commun.* **2018**, *54*, 13763–13772.
- [32] Neese, F. Calculation of the Zero-Field Splitting Tensor on the Basis of Hybrid Density Functional and Hartree-Fock Theory. *J. Chem. Phys.* **2007**, *127*, 164112.